Validation of Copernicus Sentinel-3/OLCI Level 2 LAND Integrated Water Vapour product

Niilo Kalakoski[1], Viktoria F. Sofieva[1], René Preusker[2], Claire Henocq[3], Matthieu Denisselle[3], Steffen Dransfeld[4], and Silvia Scifoni[5]

[1]Finnish Meteorological Institute, Helsinki, Finland
[2]Institute for Space Sciences, Freie Universität Berlin (FUB), Germany
[3]ACRI-ST, Sophia-Antipolis, France
[4]European Space Research Institute (ESRIN), Frascati, Italy
[5]Serco Italia SpA for European Space Agency (ESA), European Space Research Institute (ESRIN), Frascati, Italy

Correspondence: Niilo Kalakoski (niilo.kalakoski@fmi.fi)

Abstract.

Geophysical validation of the Integrated Water Vapour (IWV) from Sentinel-3 Ocean and Land Colour Instrument (OLCI) was performed as a part of "ESA/Copernicus Space Component Validation for Land Surface Temperature, Aerosol Optical Depth and Water Vapour Sentinel-3 Products" (LAW) project. The IWV was compared with reference observations from two

5 networks: GNSS (Global Navigation Satellite System) derived precipitable water vapour from the SUOMINET network and integrated lower tropospheric columns from radio-soundings from the IGRA (Integrated Radiosonde Archive) database.

Results for cloud-free matchups over land show a wet bias of 7-10% for OLCI, with a high correlation against the reference observations (0.98 against SUOMINET and 0.90 againts IGRA). Both OLCI-A and -B instruments show almost identical results, apart from an anomaly observed in camera 3 of the OLCI-B instrument, where observed biases are lower than in other

10 cameras in either instrument. The wavelength drift in sensors was investigated, and biases in different cameras were found to be independent of wavelength. Effect of cloud proximity was found to have almost no effect on observed biases, indicating that cloud-flagging in the OLCI IWV product is sufficiently robust. We performed validation of random uncertainty estimates and found them to be consistent with the statistical a posteriori estimates, but somewhat higher.

1 Introduction

15 Total column water vapour (TCWV) is one of the essential climate variables (ECV) defined by the GCOS (Global Climate Observing System) Climate Monitoring Principles (Bojinski et al., 2014). On large temporal and spatial scales, water vapour is a strong greenhouse gas, contributing to radiative climate feedback loops. Water vapour contributes also to climate and weather processes through latent heat transport (eg. Bengtsson, 2010). On smaller spatio-temporal scales, amount of water vapour in the atmosphere affects local weather conditions and hydrological cycles (Bengtsson and Hodges, 2005; Sherwood et al., 2010).

20 Because of the importance of water vapour for the climate and weather predictions, TCWV, also referred as Integrated Water Vapour (IWV) or Total Precipitable Water (TPW), has been continuously observed for decades by wide range of methods.

In addition to ground-based and In-situ observations, satellite observations using passive imagers on polar-orbiting satellites can provide daily near-global coverage. Over oceans, microwave radiometers are an established method. Over land water vapour absorption bands at 890-1000 nm wavelength band is widely used, since all surface types are bright enough at these wavelengths (Bartsch et al., 1996; Bennartz and Fischer, 2000; Albert et al., 2005).

OLCI (Ocean and Land Color Instrument) is a medium resolution imaging spectrometer, operating in the solar reflective spectral range (400 nm to 1020 nm). Two OLCI instruments, aboard Sentinel-3A (launched 2016) and -3B (launched 2018) satellites, are currently operational. The Primary mission of OLCI is the observation of sea and land surfaces, with secondary mission of providing information on atmospheric constituents. OLCI is based on the design of MERIS (Medium Resolution Imaging Spectrometer), and provides continuity with MERIS with enhanced capabilities. For detailed description of Sentinel-3 mission and OLCI instrument, see Donlon et al. (2012). OLCI level 2 IWV product for land (OL_2_LFR/OL_2_LRR) builds on heritage of water vapour algorithm designed for MERIS instruments with similar differential absorption technique.

Between January 2020 and December 2021, OLCI/Sentinel-3 IWV (included in OL_2_LFR products) was validated within the "ESA/Copernicus Space Component Validation for Land Surface Temperature, Aerosol Optical Depth and Water Vapour Sentinel-3 Products" project (referenced in the following by LAW). The aim of the project was to perform more extensive and systematic validation against ground-based measurements of the following Sentinel 3 core products: the Integrated Water Vapour included in OL_2_LFR products, Aerosol Optical Thickness included in SY_2_AOD products and Land Surface Temperature provided by SL_2_LST products.

This paper is dedicated to validation of OLCI total column water vapor data. The paper is structured in following way: Section 2 provides a brief description of the algorithm used in OLCI IWV retrieval with emphasis on the features relevant to validation work. Section 3 introduces the reference data sources used. Section 4 describes the match-up database generated as a part of LAW project, as well as the co-location criteria and screening applied to match-ups. Validation results and the discussion of results are shown in the section 5 with conclusions in section 6.

2 OLCI Integrated Water Vapour retrieval

Total column water vapour (also labeled as integrated water vapour IWV) for cloud free pixels is included in OLCI level 2 products for land (full resolution OL_2_LFR and reduced resolution OL_2_LRR) and water (OL_2_WFR/OL_2_WRR). It builds on the heritage of the retrieval algorithm designed for OLCI's precursor MERIS (Medium Resolution Imaging Spectrometer, (Rast et al., 1999; Lindstrot et al., 2012)). The water vapour column above a pixel is estimated by comparing Radiative Transfer (RT) based simulations with the corresponding OLCI measurements. The RT-simulations are approximated by a product of the atmospheric transmission (using exponential sums of pre-calculated uncorrelated k- distribution terms, (Doppler et al., 2013)) and an estimation of the scattering—absorption—interaction, quantified by a factor and stored in a look-up table (LUT). The optimisation with respect to the total column water vapour is done by a one-dimensional gradient descent (see also https://sentinel.esa.int/web/sentinel/technical-guides/sentinel-3-olci/level-2/water-vapour-retrieval, accessed on 7 March 2022).

55   Cloudy pixels are detected using standard OLCI level 2 cloud mask, which includes cloud ambiguous and cloud margin flags (see also https://sentinel.esa.int/web/sentinel/technical-guides/sentinel-3-olci/level-2/pixel-classification, accessed on 7 March 2022). For general overview of the OLCI instrument and products, see OLCI user handbook (https://sentinels.copernicus.eu/web/sentinel/user-guides/sentinel-3-olci, accessed on 7 March 2022).

3   Reference data sources

3.1   IGRA radiosoundings

The Integrated Global Radiosonde Archive (IGRA) consists of quality-controlled radiosonde and pilot balloon observations from more than 2,800 globally distributed stations, of which about 800 are currently reporting data. Version 2 of the IGRA (Durre et al., 2016) includes new data sources and quality control procedures, as well as new user-requested variables. Version 2 also includes several derived parameters, including the precipitable water vapour between surface and 500 hPa pressure level,
65   used in this study as the reference water vapour parameter. Description of the network and the quality-control measures applied can be found in Durre et al. (2018).

Soundings in IGRA database come from several sounding networks, using different radiosonde types with different processing. Due to this inhomogeneous nature, the independent uncertainty of the observation varies between stations. Wang and Zhang (2008) reports biases of around 1 kg/m^2 for different sonde types, with dry bias for capacitive polymer sondes and wet
70   bias for carbon hygristor and Goldbeater's skin hygrometers. Estimated precision of sonde-based total colunms compared to ground-based has been reported to be around 5% (Van Malderen et al., 2014).

3.2   SUOMINET GNSS network

Long-term TCWV data sets from GNSS networks are widely used in studies involving atmospheric water vapour columns. In this study, we use U.S. SuomiNet (UCAR/COSMIC) TCWV product, which consists of observations of over 400 Global
75   Positioning System (GPS) stations with near-global distribution (Ware et al., 2000). This large network provides TCWV values retrieved from consistently processed GPS measurements of the temperature- and humidity- dependent zenith path delay at a couple of hundred sites with a temporal resolution of 30 min. Analysis method and the data set is described in detail by Wang et al. (2007). While the uncertainties of the retrieval are not precisely stated by the authors, similar data sets have published accuracies of around 1–2 kg/m^2 (Gendt et al., 2004; Ge et al., 2006).

4 Match-up database and data selection

4.1 LAW match-up database

In order to facilitate validation work, ACRI-ST created a database of matchups, gathering combination of reference measurements and satellite macro-pixel collocated in time and space. The matchup database is available upon subscription LAW project web portal (https://law.acri-st.fr/home).

For IWV matchups a macro pixel of 31×31 OLCI pixels (i.e. a surface of around 10 by 10 km) with central pixel over each reference station is extracted at each overpass. All ground-based measurements acquired in a time window of +/- 3 hours are considered. Missing satellite observations were only filtered from the database in the case of operational issues or radio frequency interference (RFI) contamination. Missing satellite extractions that are due to cloud contamination or retrieval failure are included in the database, flagged with CLOUD or WV_FAIL quality flags, respectively. Automatically generated satellite extractions over each station station were associated with relevant ground-based measurements when the reference observations were available and validated. Satellite extractions included quality flags and contextual parameters present in the Sentinel-3 operational products.

Locations of IGRA and SUOMINET matchups with OLCI observations for OLCI/Sentinel-3A are shown in the Figure 1. Locations of matchups for OLCI/Sentinel-3B are similar (not shown).

4.2 Co-location criteria

For all matchups, we applied an additional quality check according to quality flags. The matchups with failed inversion (WV_FAIL flag set) or with cloud warning flag (CLOUD), were discarded. For more stringent cloud-screening, the matchups with cloud warning flags CLOUD_MARGIN and CLOUD_AMBIGUOUS were also not used. For SUOMINET matchups, only matchups with reported SUOMINET formal error of less than 2 kg/m^2 were used for the validation.

For each matchup, the satellite-reference observation pair with smallest time difference was chosen. For SUOMINET, matchups with time differences larger than 15 minutes, or nominal error larger than 2 kg/m^2 were not used. For IGRA, time differences of up to 180 minutes were allowed. For most of the comparisons, the center pixel for each macropixel, representing the closest spatial separation, was chosen.

5 Results and Discussion

5.1 Overall agreement

Comparisons were carried out separately for each instrument (OLCI-A and -B) and for each reference dataset (SUOMINET and IGRA). Results of the general comparisons are presented in Figure 2 and Table 1. All comparisons presented here use the more stringent cloud-screening criteria, discarding the matchups with OLCI observations flagged either as CLOUD_MARGIN and CLOUD_AMBIGUOUS. Likewise, only matchups over land (OLCI flag LAND) are shown.
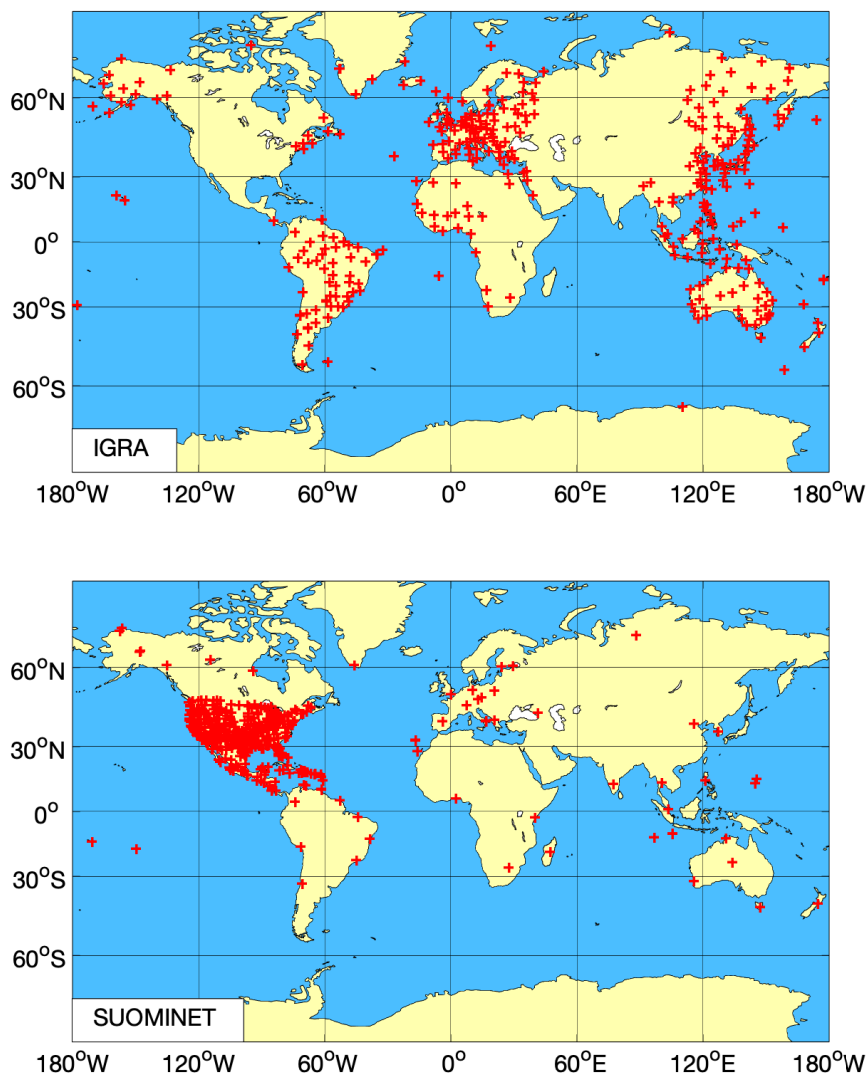
Figure 1. Locations of OLCI-A matchups with IGRA (top) and SUOMINET (bottom) networks.

110   For the cloud-free matchups over land, agreement is generally good, with very high correlation coefficients (0.98 and 0.90 for SUOMINET and IGRA, respectively). The dispersal of the differences is considerably higher for IGRA matchups, partly due to longer time differences allowed, and the drift of the sondes during the ascent. All comparisons show a positive (wet) median bias for the OLCI observations, increasing linearly with increasing total water vapour content (Figures 2 and 3). For total water contents larger than 50 kg/m^2, the bias in IGRA matchups dips closer to the zero line. As the similar dip is not

115 observed in SUOMINET comparisons, the bias reduction can be related to radiosonde data or to collocation criteria. General comparisons also indicate very good agreement between OLCI-A and -B.

Inclusion of CLOUD_MARGIN and CLOUD_AMBIGUOUS flagged observations leads to higher dispersal of differences, with large number of outliers. WATER observations, which are produced using different retrieval algorithm, severely overestimate the reference columns. WATER pixels are not strictly part of the ESA OLCI product, but are included in the files for

120 completeness. INLAND_WATER water pixels, representing rivers and lakes, similarly show wet bias and large dispersal. As the matchups are based on land-based reference observations, the number of WATER and INLAND_WATER matchups is low.

A dependency of observed biases on latitude, solar zenith angle and season was also investigated (figures A1 and A2). Results were consistent with the linear increase of wet bias seen in figures 2 and 3. The dependency observed for latitude and and solar zenith angle is related to generally higher water vapour total columns seen in low latitudes and solar zenith angles,

125 while the seasonal cycle is consistent with the over-presentation of northern hemisphere stations and higher total columns during summer months.

Table 1. Statistics of general comparisons shown in figure 2.

Parameter	SUOMINET		IGRA	
	OLCI-A	OLCI-B	OLCI-A	OLCI-B
Number of co-locations	46758	49078	20708	21021
Mean difference [kg/m^2]	1.71	1.63	2.58	2.59
Standard deviation of difference [kg/m^2]	2.93	3.07	6.22	6.41
Mean relative difference [%]	10.6	10.1	15.6	16.2
Standard deviation of relative difference [%]	21.3	22.2	44.8	49.8
Correlation coefficient	0.98	0.98	0.90	0.90

5.2 Classification of biases

While in general a validation results of OLCI-A and -B are very similar, a small anomaly in distribution of differences was observed in SUOMINET comparisons for OLCI-B camera 3, compared to the distribution for the other cameras in either in-

130 strument (Figure 4, top panels). After separating the differences by the central wavelength of the relevant instruments (Figure 4, middle and bottom panels), the anomaly in OLCI-B Camera 3 (Bottom panel, yellow line) was observed at all wavelengths, clearly distinguishable from the other cameras. This points to a conclusion that the anomaly is not due to known differential drift in camera 3, but rather due to an uncorrected instrumental issue. For more information on OLCI spectral characterization and drift of the central wavelengths, see the Sentinel Online website (https://sentinels.copernicus.eu/web/sentinel/technical-guides/

135 sentinel-3-olci/olci-instrument/spectral-characterisation-data, accessed 3 March 2022), and technical note available at the website. A small left-right bias is also seen between camera 1-5 in both instruments. This could be due to the difference in local
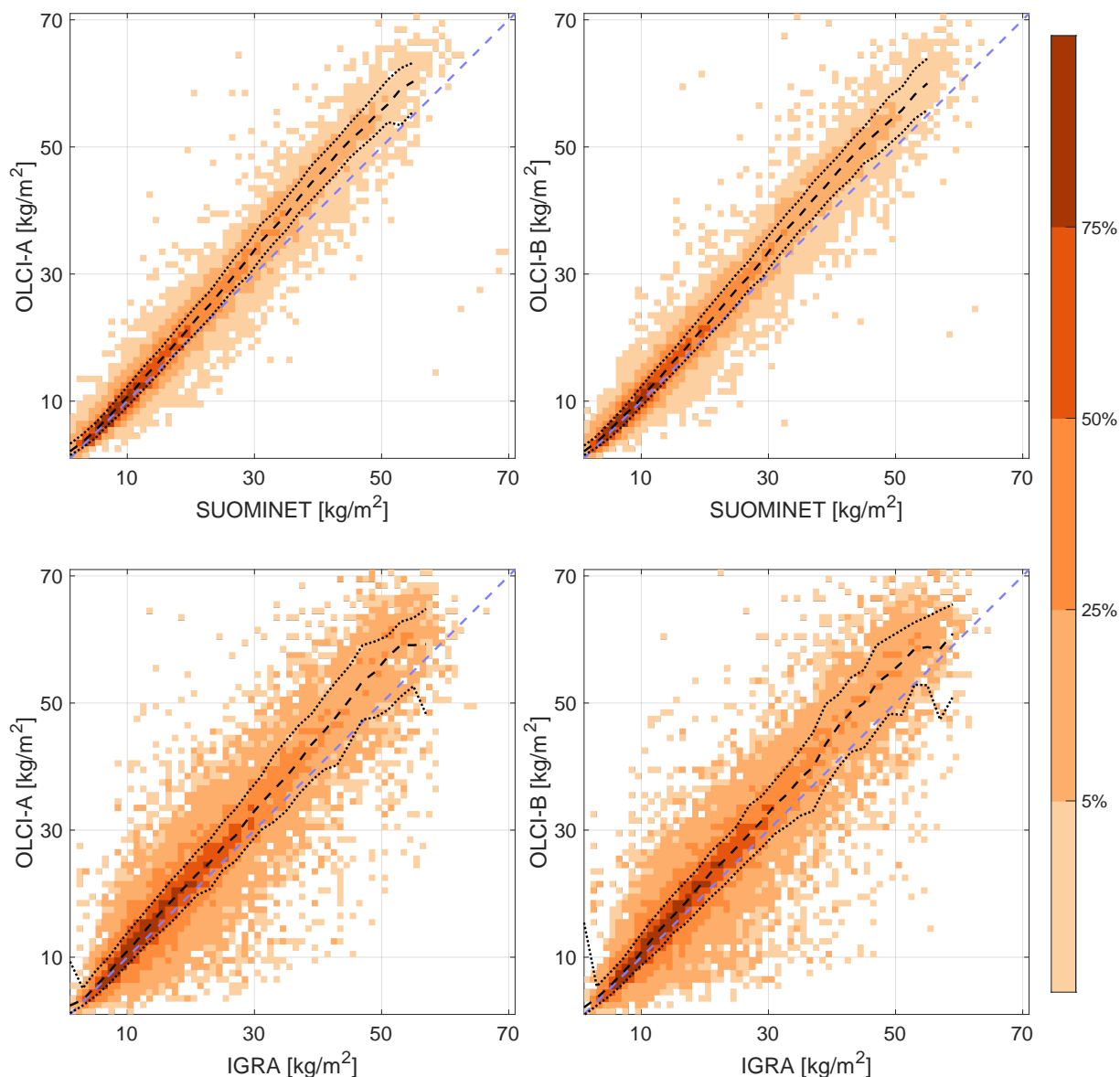
Figure 2. Density scatter plot of LAND comparisons of OLCI-A (left) and -B (right) against SUOMINET (top) and IGRA (bottom) observations, with CLOUD_MARGIN and CLOUD_AMBIGUOUS matchups removed. Color field shows the percentage of matchups in each category, with darkest colours showing the highest density of matchups. Blue dashed line shows the x = y line and the black lines median (dashed) and 16th and 84th percentiles (dotted) OLCI-A observation for each 2 kg/m^2 bin of reference observations. Linear fits of the matchups (not shown) for SUOMINET are y = 1.12x-0.31 (OLCI-A) and y = 1.11x-0.29 (OLCI-B) and for IGRA y = 1.07x+0.69 (OLCI-A) and y = 1.07x+0.64 (OLCI-B). Correlation coefficients are 0.98 (SUOMINET) and 0.90 (IGRA) for both instruments.
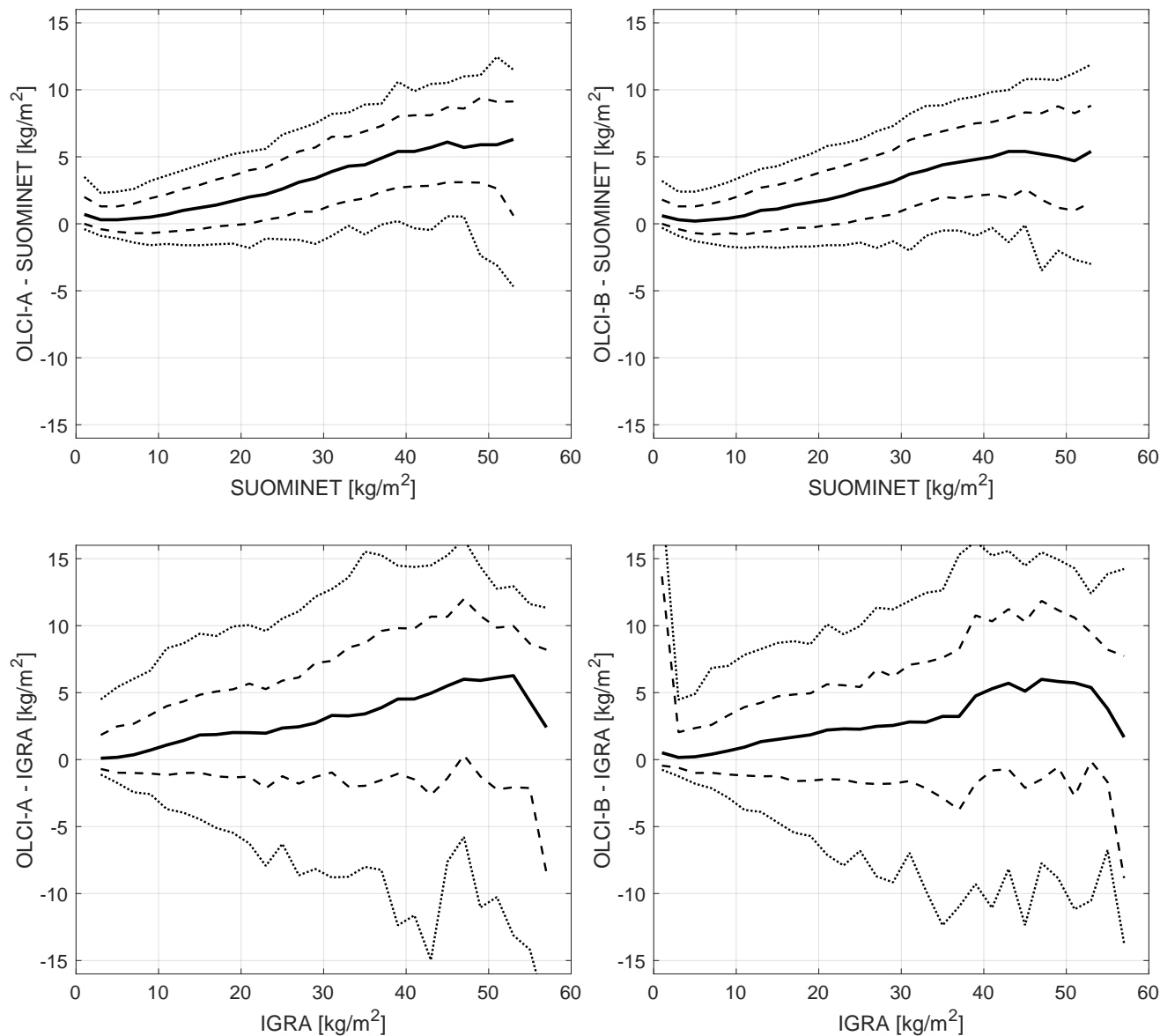
Figure 3. Difference OLCI of observations against SUOMINET (top) and IGRA (bottom) for OLCI-A (left) and OLCI-B (right). Solid line shows the median of each 2 kg/m^2 wide bin, while the dashed show the 16th and 84th percentiles and the dotted lines the 5th and 95th percentiles. Bins with less than 20 matchups were omitted from the figure.

time (about 45 minutes between cameras 1 and 5) and consequently observed total columns. Neither the left right difference or the anomaly in OLCI-B / camera 3 is observed in IGRA comparisons, due to larger dispersal of the differences.

Figure 5 shows the distribution of the differences within 31×31 pixel macropixels for cloud-free center pixels as a function
140 of distance to the closest cloud-flagged pixel. Only very small increase of median difference is seen for SUOMINET comparisons (in kg/m^2), with no increase seen for relative differences in either SUOMINET or IGRA comparisons. It should be noted that the width of the distribution increases slightly with the proximity of the cloudy pixels. However, even with this increase, we conclude that the current cloud-flagging provides robust cloud-screening, with little cloud-induced uncertainty.

5.3 Validation of error estimates

145 For the validation of random uncertainty estimates, we use the structure function method described in detail in Sofieva et al. (2021). This method is based on evaluation of the structure function, i.e., root-mean-square differences as a function of increasing spatio-temporal separation of the measurements. The limit at the zero mismatch provides the experimental estimate of random noise in the data. For the analysis shown here, we used the OLCI-A and -B data from the cloud-free SUOMINET matchups over land.

150 In order to validate the error estimates provided by the OLCI IWV algorithm, we investigated the difference of OLCI observations within the 31×31 pixel OLCI macropixel to the center pixel, and computed sample variances. RMS difference increases as a function of the distance from center (Figure 6, top-left panels). For comparison, the bottom-left panels of 6 show the mean error estimate from the OLCI product. The mean of structure function for the eight pixels around the center pixel was taken to represent the experimental uncertainty estimate for the OLCI IWV. Right panels of figure 6 show the distributions of the experimental uncertainty estimates and the estimates given by the OLCI algorithm. The distributions of the estimates

155 overlap, showing that the two estimates are consistent with each other. Experimental estimates are generally lower than the ones provided by the algorithm. This is partly caused by the 0.3 kg/m^2 increments of OLCI error estimates, which reduces the sensitivity of the OLCI estimate, especially at the lower end of the distribution. In general, the validation performed confirms the validity of the provided error estimates. However, the quantization is too coarse to provide accurate random uncertainty

160 estimates.

5.4 Surface types

Figure 7 shows the distributions of relative differences (OLCI - REF / REF) of OLCI observations against the reference observations for different surface type quality flags. OLCI observations classified as water surfaces (WATER and INLAND flags, including TIDAL with WATER) considerably larger bias and dispersal than those classified as land surfaces (LAND

165 flag, including TIDAL with LAND). Since the reference observation sites are located on land, the number of water matchups is small, and necessarily limited to being very close to coastline. While the number of non-land matchups is small, results indicate that the water pixels in coastal areas should be used with caution. This is an expected and known issue, since the very dark water surface leads to a signal return that is predominantly not influenced by the full atmospheric column. Instead it is dominated by a complex interaction of aerosol layer height, aerosol optical thickness, water leaving radiance and sun glint.
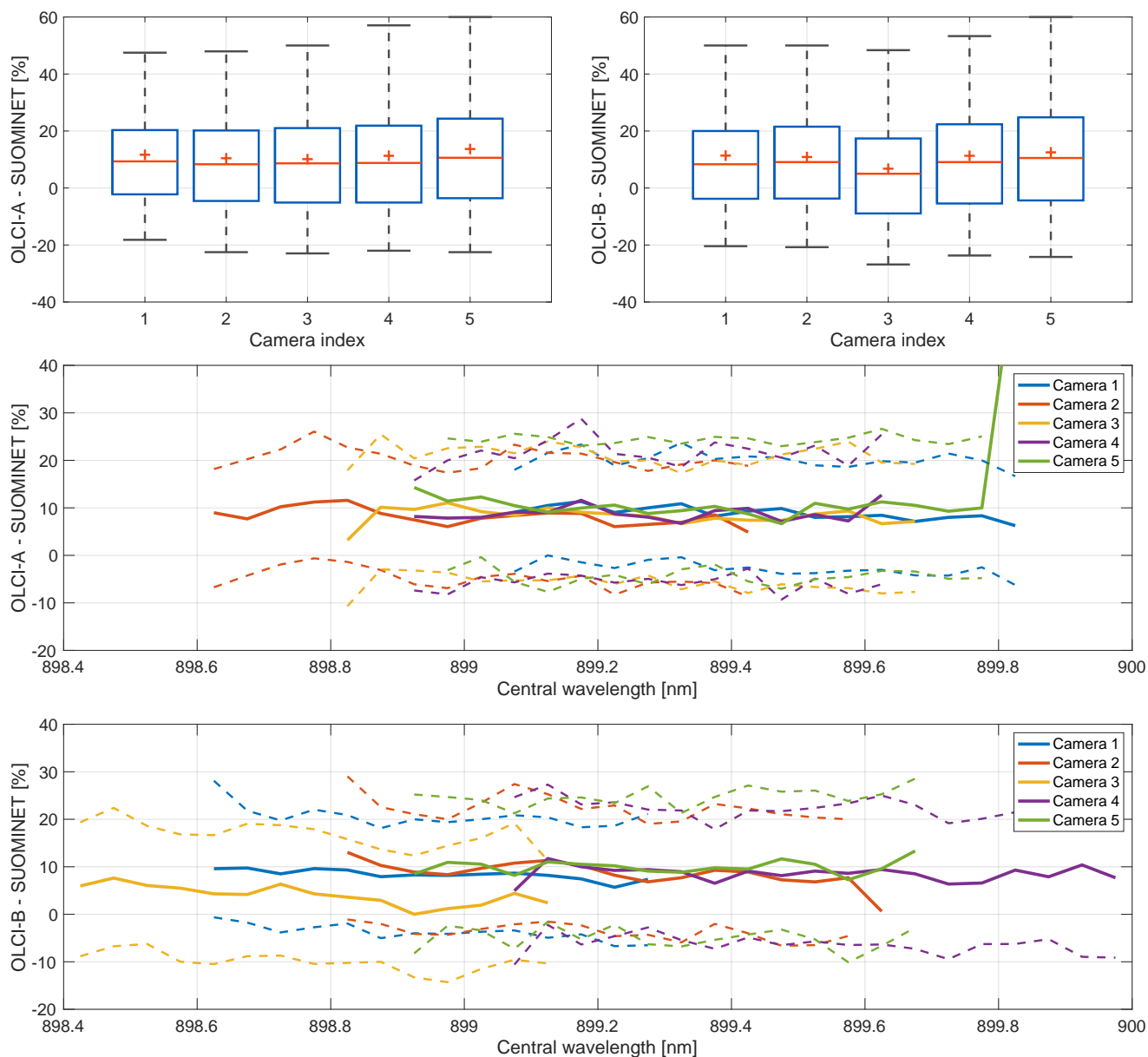
Figure 4. Dependency of OLCI - SUOMINET relative difference on camera index. Top row: Distributions of relative differences for OLCI-A (left) and OLCI-B (right) match-ups with SUOMINET observations for OLCI cameras 1-5. Red lines show the medians of the distributions and blue boxes the 16th and 84th percentiles of the distribution with black whiskers showing the 2.5th and 97.5th percentiles. Red crosses show the means of the distributions. Middle and bottom rows: Relative difference as a function of central wavelength of the detector for OLCI-A (middle panel) and OLCI-B (bottom panel). Colors represent cameras 1-5 (see legend) and the solid and dashed lines represent median and the interpercentile range (16th-84th) percentiles, respectively.
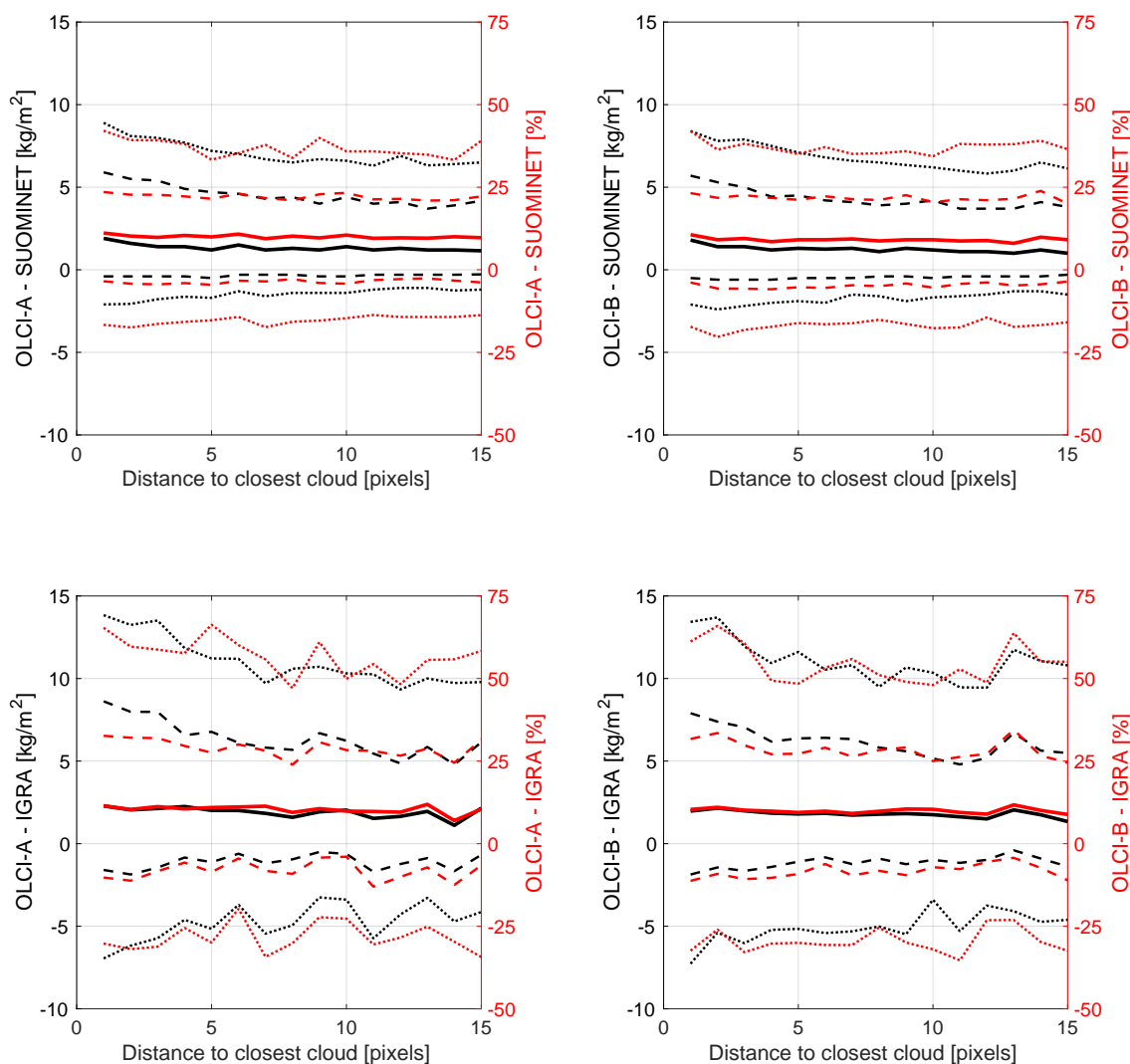
Figure 5. Dependency of observed OLCI difference against SUOMINET (Top) and IGRA (bottom) observations to distance to closest cloud-flagged pixel for OLCI-A and -B (left and right columns, respectively). Black lines show the difference in kg/m^2, while the red lines show the relative difference in percent. Solid line shows the median of each 2 kg/m^2 wide bin, while the dashed show the 16th and 84th percentiles and the dotted lines the 5th and 95th percentiles.
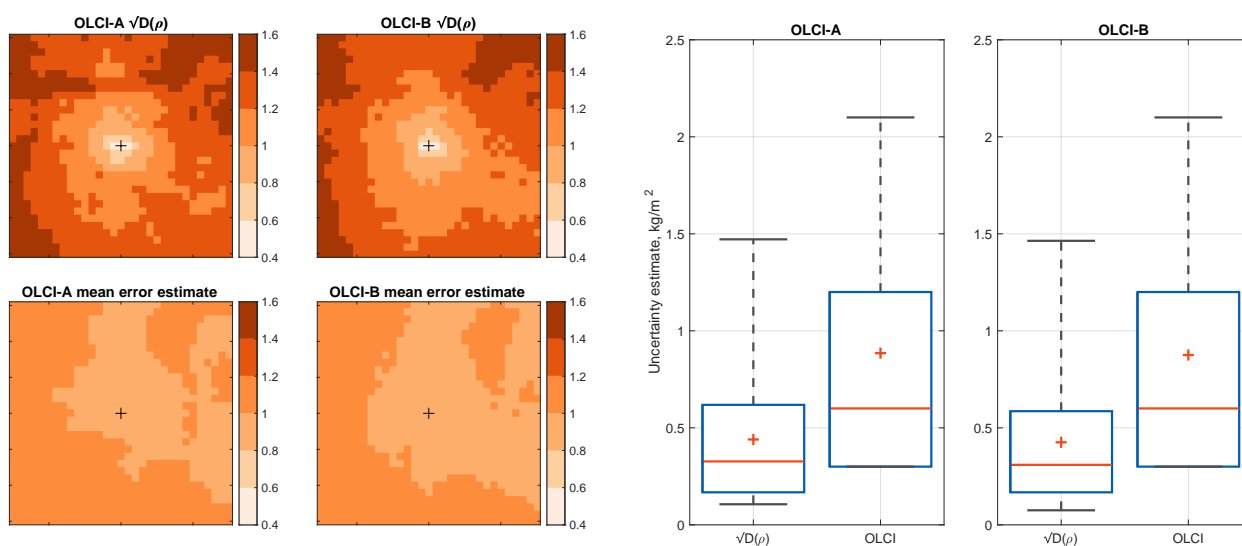
Figure 6. Left panels: Structure function ($\sqrt{D(\rho)}$ in kg/m^2) within macropixel, compared to center of the macropixel (Top) and the square root of mean error estimate of corresponding OLCI pixels (bottom). Rigth panels: Distribution of experimental uncertainty estimates (8 pixels around the center of the macropixel) using the structure function method $\sqrt{D(\rho)}$ and the IWV uncertainty estimates from inversion algorithm. Red lines show the medians of the distributions and blue boxes the 16th and 84th percentiles of the distribution with black whiskers showing the 5th and 95th percentiles. Red crosses show the means of the distributions.
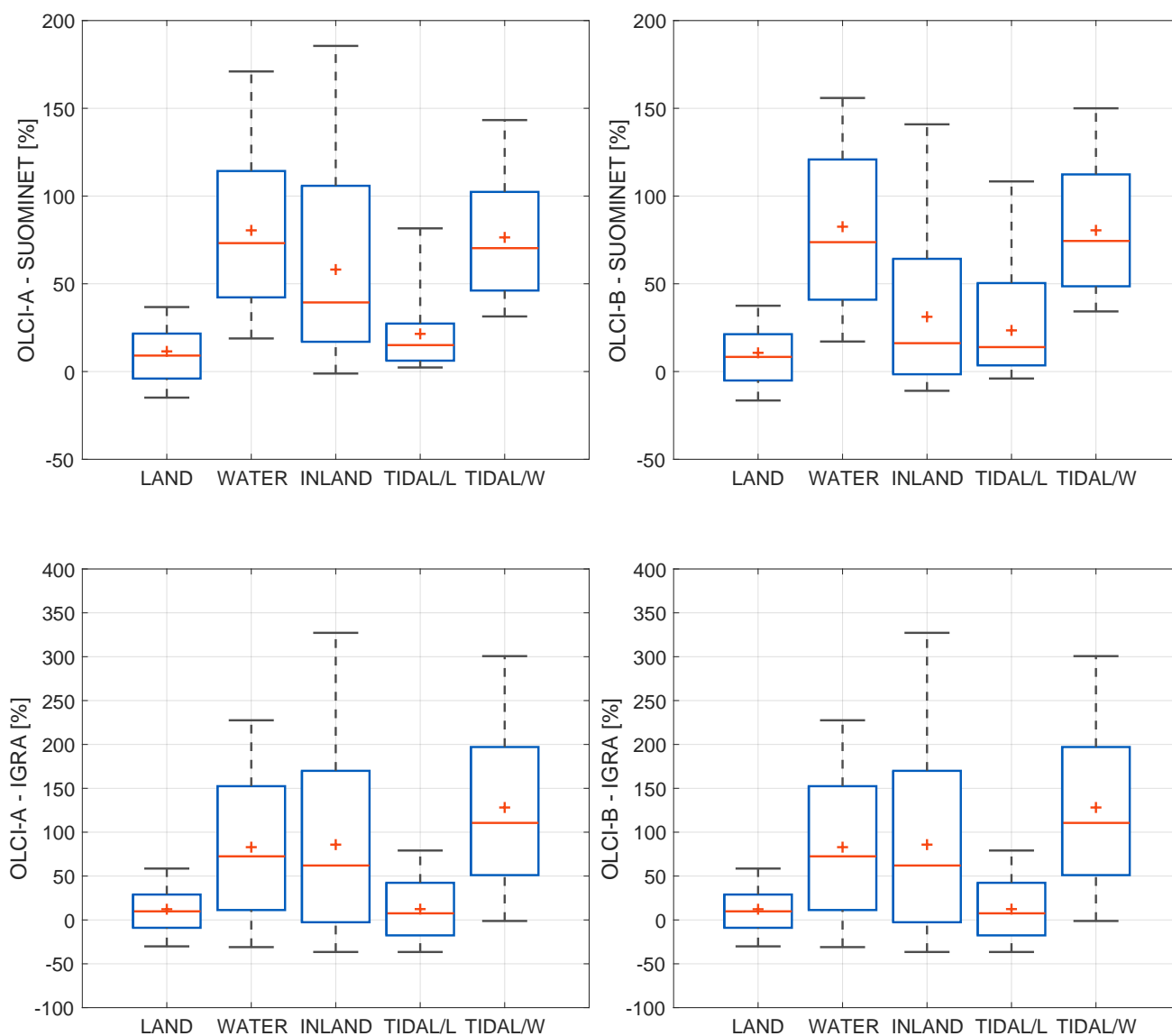
Figure 7. Distributions of relative differences [in %] of OLCI-A (left) and OLCI-B (right) observations against SUOMINET (top) and IGRA (bottom) for different surface types. TIDAL matchups are shown separately for LAND and WATER. LAND distribution includes TIDAL/L matchups and WATER distribution INLAND and TIDAL/W matchups. Red lines show the medians of the distributions and blue boxes the 16th and 84th percentiles of the distribution with black whiskers showing the 5th and 95th percentiles. Red crosses show the means of the distributions. Note the different y-scales for SUOMINET and IGRA distributions.

6 Conclusions

OLCI IWV was validated against two reference datasets, SUOMINET GNSS observations and IGRA integrated radiosonde columns. High correlation with the reference observations (0.98 for SUOMINET and 0.90 for IGRA) was observed for both OLCI-A and -B, with all comparisons showing a wet bias of 7-10%. Notably, the results of the general comparisons were very similar for OLCI-A and B.

In more detailed comparisons, wavelength dependency of an observed anomaly in OLCI-B/camera 3 was investigated, showing that the anomaly is independent of the central wavelength of the relevant sensor. This indicates that the cause of the anomaly is not the wavelength drift of the sensors in camera 3. Proximity of clouds within the macropixel was shown to have little effect on the observed differences, confirming the robustness of cloud-flags provided with the OLCI product.

Error estimates of the OLCI product were compared to an experimental estimate of random uncertainty. Comparisons indicate that the OLCI estimates were consistent with the experimental estimates, but generally higher. This is partly due to large increment (0.3 kg/m^2) of the reported OLCI error estimates.

As an outcome of the validation work carried out within the LAW project, three main recommendations were submitted: 1.) Possibility of reducing the wet bias using additional OLCI channels (see Preusker et al., 2021) should be investigated, 2.) correction to the anomaly observed in Camera 3 / OLCI-B should be implemented, and 3.) uncertainty estimates should be revisited, preferably with smaller increments for better characterization.

Data availability. Matchup data base containing the data used for this work is available on subscription at https://law.acri-st.fr/home

Author contributions. N.K. and V.S. planned the validation approach. C.H. and M.D. produced the matchup database. N.K. performed the analysis and prepared the manuscript with contributions from all authors.

Competing interests. The authors declare that they have no conflict of interest.

Acknowledgements. The work presented here was funded by "ESA/Copernicus Space Component Validation for Land Surface Temperature, Aerosol Optical Depth and Water Vapour Sentinel-3 Products" project.

Authors would like to thank UCAR and Suominet project for the SUOMINET data and NOAA for the IGRA data.

FMI thanks the Academy of Finland (Centre of Excellence in Inverse Modelling and Imaging).

References

195 Albert, P., Bennartz, R., Preusker, R., Leinweber, R., and Fischer, J.: Remote sensing of atmospheric water vapor using the moderate resolution imaging spectroradiometer, Journal of Atmospheric and Oceanic Technology, 22, 309–314, 2005.

Bartsch, B., Bakan, S., and Fischer, J.: Passive remote sensing of the atmospheric water vapour content above land surfaces, Advances in Space Research, 18, 25–28, https://doi.org/https://doi.org/10.1016/0273-1177(95)00285-5, satellite data for atmosphere, continent and ocean research, 1996.

200 Bengtsson, L.: The global atmospheric water cycle, Environmental Research Letters, 5, 025 202, 2010.

Bengtsson, L. and Hodges, K. I.: On the impact of humidity observations in numerical weather prediction, Tellus A: Dynamic Meteorology and Oceanography, 57, 701–708, 2005.

Bennartz, R. and Fischer, J.: A modified k-distribution approach applied to narrow band water vapour and oxygen absorption estimates in the near infrared, Journal of Quantitative Spectroscopy and Radiative Transfer, 66, 539–553, https://doi.org/https://doi.org/10.1016/S0022-4073(99)00184-3, 2000.

205

Bojinski, S., Verstraete, M., Peterson, T. C., Richter, C., Simmons, A., and Zemp, M.: The concept of essential climate variables in support of climate research, applications, and policy, Bulletin of the American Meteorological Society, 95, 1431–1443, 2014.

Donlon, C., Berruti, B., Buongiorno, A., Ferreira, M.-H., Féménias, P., Frerick, J., Goryl, P., Klein, U., Laur, H., Mavrocordatos, C., et al.: The global monitoring for environment and security (GMES) sentinel-3 mission, Remote sensing of Environment, 120, 37–57, 2012.

210 Doppler, L., Preusker, R., Bennartz, R., and Fischer, J.: K-bin and k-IR: K-distribution methods without correlation approximation for non-fixed instrument response function and extension to the thermal infrared-Applications to satellite remote sensing, https://doi.org/10.1016/j.jqsrt.2013.09.001, 2013.

Durre, I., Xungang, Y., Vose, R. S., Applequist, S., and Arnfield, J.: Integrated Global Radiosonde Archive (IGRA), Version 2, https://doi.org/DOI:10.7289/V5X63K0Q, 2016.

215 Durre, I., Yin, X., Vose, R. S., Applequist, S., and Arnfield, J.: Enhancing the data coverage in the Integrated Global Radiosonde Archive, Journal of Atmospheric and Oceanic Technology, 35, 1753–1770, 2018.

Ge, M., Gendt, G., Dick, G., Zhang, F., and Rothacher, M.: A new data processing strategy for huge GNSS global networks, Journal of Geodesy, 80, 199–203, 2006.

Gendt, G., Dick, G., Reigber, C., Tomassini, M., Liu, Y., and Ramatschi, M.: Near real time GPS water vapor monitoring for numerical weather prediction in Germany, Journal of the Meteorological Society of Japan. Ser. II, 82, 361–370, 2004.

220

Lindstrot, R., Preusker, R., Diedrich, H., Doppler, L., Bennartz, R., and Fischer, J.: 1D-Var retrieval of daytime total columnar water vapour from MERIS measurements, 5, 631–646, https://doi.org/10.5194/amt-5-631-2012, 2012.

Preusker, R., Carbajal Henken, C., and Fischer, J.: Retrieval of Daytime Total Column Water Vapour from OLCI Measurements over Land Surfaces, Remote Sensing, 13, 932, 2021.

225 Rast, M., Bezy, J. L., and Bruzzi, S.: The ESA Medium Resolution Imaging Spectrometer MERIS a review of the instrument and its mission, 20, 1681–1702, https://doi.org/10.1080/014311699212416, 1999.

Sherwood, S., Roca, R., Weckwerth, T., and Andronova, N.: Tropospheric water vapor, convection, and climate, Reviews of Geophysics, 48, 2010.

Sofieva, V. F., Lee, H. S., Tamminen, J., Lerot, C., Romahn, F., and Loyola, D. G.: A method for random uncertainties validation and
probing the natural variability with application to TROPOMI on board Sentinel-5P total ozone measurements, Atmospheric Measurement
Techniques, 14, 2993–3002, 2021.

Van Malderen, R., Brenot, H., Pottiaux, E., Beirle, S., Hermans, C., De Mazière, M., Wagner, T., De Backer, H., and Bruyninx, C.: A
multi-site intercomparison of integrated water vapour observations for climate change analysis, Atmospheric Measurement Techniques,
7, 2487–2512, 2014.

Wang, J. and Zhang, L.: Systematic errors in global radiosonde precipitable water data from comparisons with ground-based GPS measurements, Journal of Climate, 21, 2218–2238, 2008.

Wang, J., Zhang, L., Dai, A., Van Hove, T., and Van Baelen, J.: A near-global, 2-hourly data set of atmospheric precipitable water from
ground-based GPS measurements, Journal of Geophysical Research: Atmospheres, 112, 2007.

Ware, R. H., Fulker, D. W., Stein, S. A., Anderson, D. N., Avery, S. K., Clark, R. D., Droegemeier, K. K., Kuettner, J. P., Minster, J. B.,
and Sorooshian, S.: SuomiNet: A real-time national GPS network for atmospheric research and education, Bulletin of the American
Meteorological Society, 81, 677–694, 2000.
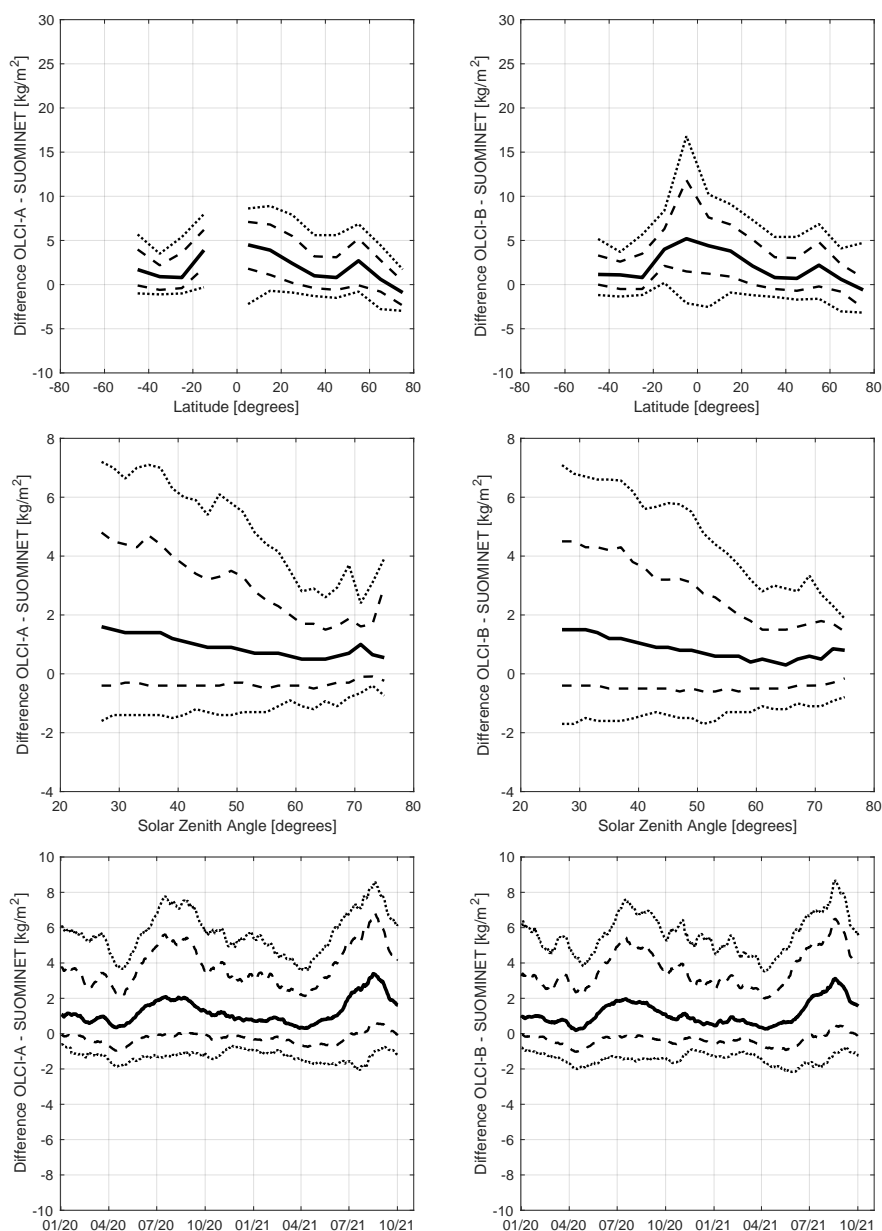
Figure A1. Difference OLCI-A (left) and -B (right) of observations against SUOMINET as a function of latitude (top row), Solar zenith angle (middle row) and time (bottom row). Solid line shows the median of each 2 kg/m^2 wide bin, while the dashed show the 16th and 84th percentiles and the dotted lines the 5th and 95th percentiles. Bins with less than 20 matchups were omitted from the figure.
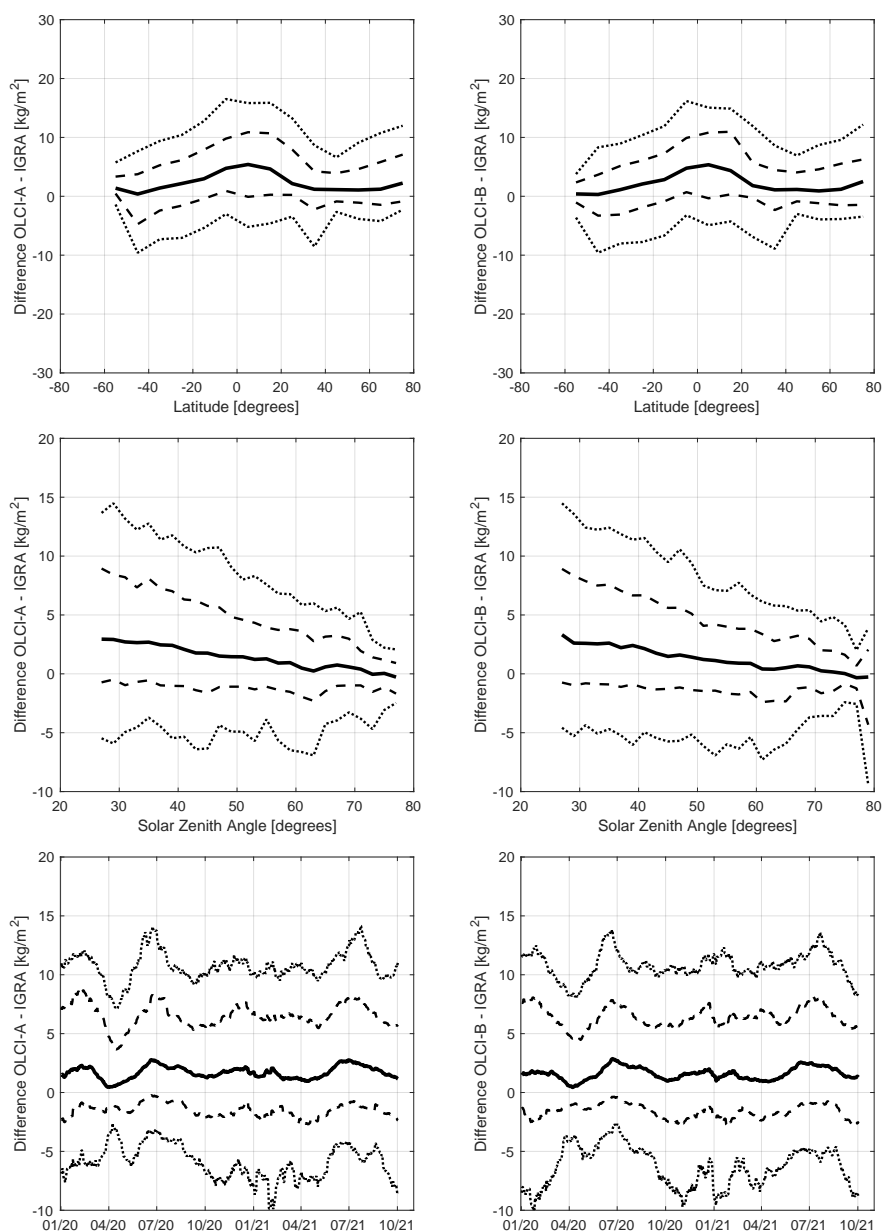
Figure A2. Difference OLCI-A (left) and -B (right) of observations against IGRA as a function of latitude (top row), Solar zenith angle (middle row) and time (bottom row). Solid line shows the median of each 2 kg/m^2 wide bin, while the dashed show the 16th and 84th percentiles and the dotted lines the 5th and 95th percentiles. Bins with less than 20 matchups were omitted from the figure.